Numerical phase space optics methods and applications to the analysis of fiber coupling efficiency in atmospheric turbulence

Yousef K. Chahine[a,*], Ferrill Rushton[b], Brian E. Vyhnalek[a], and Sarah A. Tedder[a]

[a]NASA Glenn Research Center, Optics and Photonics Branch, Cleveland, Ohio, 44135
[b]University of California San Diego, La Jolla, California

ABSTRACT

A fundamental requirement of free-space optical communication is the ability to efficiently couple atmospherically distorted light from a telescope to a detector. A numerical method is presented for modeling fiber-based receiver performance in atmospheric conditions based on phase space optics which does not rely on Monte Carlo methods. This method is employed to analyze the waveguide insertion loss and optimal coupling geometry in atmospheric conditions for step-index fibers, graded-index fibers, and photonic lanterns with and without tilt compensation and central obscurations in the telescope.

Keywords: free-space optical communication, atmospheric turbulence, phase space optics, Wigner distribution function, optical fibers, fiber devices

1. INTRODUCTION

Free space optical links have a number of potential benefits over traditional radio frequency (RF) systems including minimal diffraction loss over long-range links and wide available communications bandwidth. At the same time, free-space optical links introduce significant new challenges including strict beam pointing requirements and the susceptibility of optical transmission to degradation from turbulence in the Earth's atmosphere. The former plays a prominent role in determining the power in bucket at the receiving telescope, while the latter can affect both total power in the aperture as well as the efficiency of coupling that energy through the receiver optics to a detector. For photon-starved links, the receiver design must be optimized to obtain the highest efficiency possible while simultaneously working under constraints imposed by photonic systems used for optical processing and detection.[1–3]

Fiber-based optical receiver systems which couple to a very large multi-mode fiber (MMF) to deliver light to the detectors may be analyzed within a framework of geometrical optics combined with an analysis of the encircled energy of the average point-spread function (PSF) after propagation in the atmosphere. Such a treatment is insufficient for systems coupling to single-mode fiber (SMF). Adequate techniques include wave optics based analyses via overlap integrals relating the coherent optical transfer function (OTF) and/or pupil-plane mutual coherence function (MCF) of the incident light and the fundamental mode of the fiber,[4,5] though experimental investigations of more complex systems are often guided by an analysis of the PSF and/or Strehl ratio.[6]

The intermediate regime where only partial spatial mode-filtering is required—so that few-mode fiber (FMF) or low multi-mode fiber devices such as photonic lanterns may be employed—has only recently received significant study.[7,8] Theoretical treatments of free-space coupling to very few-mode fibers (less than 10 guided modes) have been presented following the treatments of SMF coupling, sometimes with simplifying approximations introduced for the higher order fiber modes.[9,10] More complex mode-limited systems have been studied via Monte Carlo simulations of atmospheric effects using randomly generated phase screens. The latter approach is especially effective for active systems including simulation of closed-loop adaptive optics.[11,12]

In this paper we employ a phase space representation, specifically the Wigner distribution function, to study fiber coupling efficiency and coupling geometry in the transition from single-mode to multi-mode systems operating over free-space atmospheric channels. Phase space methods, though well-known in radiometry and non-imaging optics, appear to be less widespread in the field of free-space optical communications due to the historical

*yousef.k.chahine@nasa.gov

connection between atmospheric optics and the problem of imaging through the atmosphere. Nevertheless, phase space methods are well-aligned to the goals of free-space optical communications as optical communication channels are ultimately governed by the same power transfer and thermodynamic principles which are of primary concern in radiometry and non-imaging optics.[13,14]

A phase space analysis of the optimal efficiency obtainable for passively coupled fiber-based receivers with a limited number of guided modes was recently presented in Ref. 15. This analysis was based on a detailed study of the Wigner distribution describing light after propagation through the atmosphere with specific consideration given to the coupling efficiency into step-index fibers. In this paper, we extend this work with a shift in focus to an analysis of the mode structure of the waveguide, and the impact of mode structure on the optimization and tolerances in the coupling geometry for mode-limited systems which must operate at peak efficiency in a range of atmospheric conditions.

In Section 2, we outline a general framework of numerical phase space optics for modeling optical transmission on free-space links including a discussion of the types of systems for which such modeling is appropriate. In Section 3, we analyze the Wigner distributions associated to waveguide modes for step-index fibers, graded-index fibers, and several photonic lantern structures. A calculation of the Wigner distributions describing incident light after propagation through atmospheric turbulence is presented in Section 3.2, including a study of the effects of wavefront tilt compensation and pupil obscurations. These analyses are combined to investigate the impact of mode structure on coupling efficiency with and without a central obscuration in the telescope (Section 3.3). Optimization and tolerances in the input numerical aperture (NA) are characterized for step-index fibers, graded-index fibers, and photonic lanterns in a range of atmospheric conditions characterized by the ratio of telescope diameter D to atmospheric coherence diameter r_0 (Section 3.4).

2. METHOD

2.1 Discrete Wigner transform

The Wigner transform is one of the fundamental tools in phase space optics. The Wigner transform of a 2-dimensional complex-valued signal $\psi \in L^2(\mathbb{R}^2)$ is a real-valued function defined by[16]

$$\mathcal{W}[\psi](\vec{x},\vec{\xi}) = \iint \psi^*\Big(\vec{x}-\frac{\vec{r}}{2}\Big)\psi\Big(\vec{x}+\frac{\vec{r}}{2}\Big)e^{-2\pi i\vec{\xi}\cdot\vec{r}}\,d^2\vec{r}. \tag{1}$$

The transform faithfully represents the signal ψ in the sense that it can be inverted to obtain the original signal ψ up to a global phase. In addition to defining the transform of individual signals, one can also define the Wigner transform of a statistical ensemble $\{(\psi_i,\rho_i)\}_{i\in\mathbb{N}}$—with weights $\rho_i \geq 0$ representing a probability distribution $\sum_i \rho_i = 1$—as the average of the Wigner transforms $\mathcal{W}[\{(\psi_i,\rho_i)\}] = \sum_i \rho_i \mathcal{W}[\psi_i]$.[17] If the statistics of the signals are known, specifically the local auto-correlation function $\mu(\vec{x}_1,\vec{x}_2) = \langle\psi^*(\vec{x}_1)\psi(\vec{x}_2)\rangle$ (or the MCF in the context of monochromatic optical fields), then by linearity of the integral (1) the Wigner transform of the ensemble may be calculated as the Fourier transform of the MCF referenced to the midpoint $\mu_{\vec{x}}(\vec{r}) = \mu(\vec{x}-\vec{r}/2,\vec{x}+\vec{r}/2)$.

Numerical implementation of the Wigner transform for a discretely sampled signal on a rectangular grid can be accomplished by identifying the Wigner transform as a family of Fourier transforms

$$\mathcal{W}[\psi](\vec{x},\vec{\xi}) = \mathcal{F}[\mu_{\vec{x}}(\vec{r})](\vec{\xi}) \tag{2}$$

parameterized by the position vector $\vec{x}$ defining the center of the conjugate-centrosymmetric function $\mu_{\vec{x}}(\vec{r}) = \psi^*(\vec{x}-\vec{r}/2)\psi(\vec{x}+\vec{r}/2)$. Numerical evaluation proceeds by forming the function $\mu_{\vec{x}}(\vec{r})$ for each point $\vec{x}$ in the sampling grid and approximating (2) using a discrete Fourier transform (DFT).

A number of alternative definitions of the discrete Wigner transform—known as the discrete Wigner-Ville distribution (DWVD) in the context of time-frequency analysis—have been introduced.[18,19] The version above, first studied by Claasen and Mecklenbräuker,[20] has the benefit of both computational and memory efficiency, these representing primary considerations for a useful numerical implementation of the Wigner transform of a 2D optical signal. A general treatment of the sampling theory for the Wigner transform can be found in references on time-frequency analysis and the DWVD.[20–22] Appendix A outlines some practical considerations for efficiently sampling 2D optical signals when numerically evaluating the discrete Wigner transform.

2.2 Properties of the optical Wigner distribution function

Henceforth we consider complex-valued signals $\psi(\vec{x}) = \psi(\vec{x}; z)$ which represent a single electric field component of a monochromatic, linearly-polarized traveling wave $E(\vec{x}, z, t) = \mathrm{Re}[\psi(\vec{x}; z)e^{i(kz-\omega t)}]$ with wavelength λ, wavenumber $k = 2\pi/\lambda$, and angular frequency ω. Correspondingly, we shall work in terms of the Wigner distribution defined in canonically conjugate phase space coordinates $\mathbf{u} = (\vec{q}, \vec{p})$ by[23]

$$W_\psi(\vec{q}, \vec{p}) = \frac{1}{\lambda^2}\mathcal{W}[\psi]\Big(\vec{q}, \frac{\vec{p}}{\lambda}\Big). \tag{3}$$

The optical momentum $p = |\vec{p}|$ associated to a transverse spatial frequency $\kappa = kp$ of the optical field shall be referred to as the angle variable as an aid to physical intuition, though it should be stressed that individual points $(\vec{q}, \vec{p})$ carry no physical meaning and the angle interpretation (as in ray optics) is appropriate only within the small angle approximation $p = n \sin\theta_z \simeq n\theta_z$ where θ_z is the angle of a ray with the optical axis. Several well-known properties of the Wigner distribution used extensively in this work are summarized below.[23,24]

Marginal relations. Integrating the Wigner distribution over all optical momenta (or all of space) yields the power density in the conjugate domain

$$|\psi(\vec{q})|^2 = \iint W_\psi(\vec{q}, \vec{p})\, d^2\vec{p}, \qquad |\tilde{\psi}(\vec{p}/\lambda)|^2 = \lambda^2 \iint W_\psi(\vec{q}, \vec{p})\, d^2\vec{q} \tag{4}$$

where $\tilde{\psi} = \mathcal{F}[\psi]$ denotes the Fourier transform. Integrating over all of phase space yields the L^2-norm $|\langle\psi, \psi\rangle|^2$.

Moyal formula. The squared-modulus of the L^2 Hermitian inner product of two optical fields ψ, φ is given by the overlap integral of the real-valued Wigner distributions

$$|\langle\varphi, \psi\rangle|^2 = \lambda^2 \iiiint W_\varphi(\mathbf{u}) W_\psi(\mathbf{u}) d^4\mathbf{u}. \tag{5}$$

By linearity, if one of the Wigner distributions is associated to a statistical ensemble $W = \sum \rho_i W_{\psi_i}$ the overlap integral above represents the ensemble average of the squared moduli on the left.

First-order systems (linear canonical transformations). In the Fresnel approximation, the evolution of ψ through any first-order optical system described by a 4×4 symplectic ray transfer matrix S in $Sp(4, \mathbb{R})$ can be obtained by precomposition with the inverse linear coordinate transformation $(S^{-1})^* W_\psi(\mathbf{u}) = W_\psi(S^{-1}\mathbf{u})$.

Optical misalignments (affine symplectic maps). Decentering and tilt of the light relative to the optical axis can be represented by a translation of the underlying coordinates $\mathbf{u} \mapsto \mathbf{u} + \mathbf{v}$. The translation vector is given by $\mathbf{v} = (\vec{q}_s, \vec{p}_t)$ where $\vec{q}_s = (q_x, q_y)$ represents the transverse shift of the axis and $\vec{p}_t = (\cos\theta_x, \cos\theta_y)$ represents the tilt of the axis in terms of the direction cosines $(\theta_x, \theta_y \simeq \pi/2)$. Propagation through a first-order optical system including free-space Fresnel propagation, thin lenses, and misalignments can be represented by extending the linear canonical transformations to the group of 5×5 matrices A in the affine symplectic group

$$A = \begin{pmatrix} S & \mathbf{v} \\ \mathbf{0} & 1 \end{pmatrix} \tag{6}$$

acting on the phase space embedded as a hyperplane $\mathbf{u} \mapsto (\mathbf{u}, 1)$ in $\mathbb{R}^5$.

Optical Liouville theorem. If two fields φ and ψ are not co-located in the same plane but can be reconciled to a common plane via propagation through first-order optical systems described by affine symplectic maps A_1, A_2, a change of variables yields

$$\lambda^2 \iiiint W_\varphi(A_1^{-1}\mathbf{u}) W_\psi(A_2^{-1}\mathbf{u}) d^4\mathbf{u} = \lambda^2 \iiiint W_\varphi(\mathbf{u}) W_\psi(A_1 A_2^{-1}\mathbf{u}) d^4\mathbf{u} \tag{7}$$

since A_1, A_2 are linear maps with determinant 1 (and hence also have Jacobian determinant 1).

2.3 Algorithm

The algorithm for modeling the propagation and coupling of light through an optical system is as follows:

1. Calculate the Wigner distributions W_1, W_2 of the incident light and optical modes in the system, either via the coherent field ψ or via the MCF $\mu(\vec{x}_1, \vec{x}_2)$ for a partially coherent field. This is done in a convenient reference plane where the field is known (e.g. at the transmitter, telescope aperture, or optical fiber).

2. Compute the change of coordinates A_1, A_2 describing propagation to a common plane (e.g. a telescope focal plane or fiber entrance plane), including any pointing offsets and misalignments to be modeled.

3. Numerically approximate the coupling integral (7) as a sum

$$\lambda^2(\Delta q)^2(\Delta p)^2 \sum_{i,j,k,l} W_1(\mathbf{u}_{ij,kl}) W_2(A_1 A_2^{-1} \mathbf{u}_{ij,kl}) \tag{8}$$

   by interpolating the Wigner distribution W_2 on the grid $\mathbf{u}'_{ij,kl} = A_1 A_2^{-1} \mathbf{u}_{ij,kl}$ determined by transforming the original grid $\mathbf{u}_{ij,kl} = (q_i, q_j, p_k, p_l)$ used to sample the discrete Wigner transform W_1.

There are several features of this algorithm which differentiate it from other methods. The first is that all propagation effects falling within the domain of the affine symplectic maps are modeled by interpolating the original Wigner distribution on a grid obtained from the original grid by vectorized matrix multiplication of 5×5 matrices. After the initial computation of the Wigner transform there is no need for computing Fresnel diffraction integrals or implementing boundary conditions as in traditional numerical beam propagation methods. Of course, the initial Wigner transform has a significant computational cost and must be sampled well enough to ensure sufficient accuracy of the interpolation. For statistical ensembles this holds also for the propagation of the MCF yielding a natural method for modeling the propagation of partially coherent fields through linear optical systems.

Another feature of this algorithm is the fact that the squared modulus of the Hermitian inner product of two optical fields is a bilinear function of the associated Wigner functions (5). This linearity enables the efficient calculation of the coupling efficiency into few-mode and even highly multi-mode waveguides within a fully wave-optical framework. This is done by forming a waveguide distribution $\overline{W} = \sum_m W_{\varphi_m}$ prior to computing the overlap integral.[15] In contrast, if one calculates the coupling integral directly using the complex mode fields φ_m, one must calculate the overlap integral for each mode individually. The waveguide distribution $\overline{W}$ has the additional benefit of characterizing aggregate properties of the light propagating in few-mode and multi-mode waveguides which are not directly apparent from a decomposition into guided modes (*cf.* Sec. 3.1).

On the other hand, modeling propagation effects which fall outside the domain of the affine symplectic maps can be inefficient using the Wigner distribution. For example, multiplication of the field ψ by a phase screen as in the split-step beam propagation method[25] takes the form of a convolution of the Wigner distribution. Wigner distribution methods are particularly effective for partially coherent fields and multi-mode systems where the statistics of the optical fields are known in a plane which can be related to the plane of interest via a first-order optical system (i.e. a linear canonical transformation).

3. PHASE SPACE ANALYSIS OF FIBER COUPLING AFTER PROPAGATION THROUGH THE ATMOSPHERE

This section develops applications of the method of Section 2 to the analysis of fiber-coupled optical receivers operating over atmospheric channels. A general picture of free-space optical systems from the perspective of phase space distributions is illustrated in Figure 1. In the geometrical optics limit of incoherent light coupling into very large multi-mode fibers, the Wigner function for both the incident light in the pupil and light in the waveguide can be approximated by a constant distribution on a phase space domain Ω with étendue $G = \mathrm{vol}(\Omega) \gg \lambda^2$ often with hard system cutoffs in numerical aperture p_0 and radius q_0. In the opposite limit of an ideal free-space channel with diffraction-limited optics coupling to SMF, the Wigner distribution for a plane wave illuminated circular aperture exhibits a hard cutoff at the pupil radius q_0 but has a complicated angular spread in p with

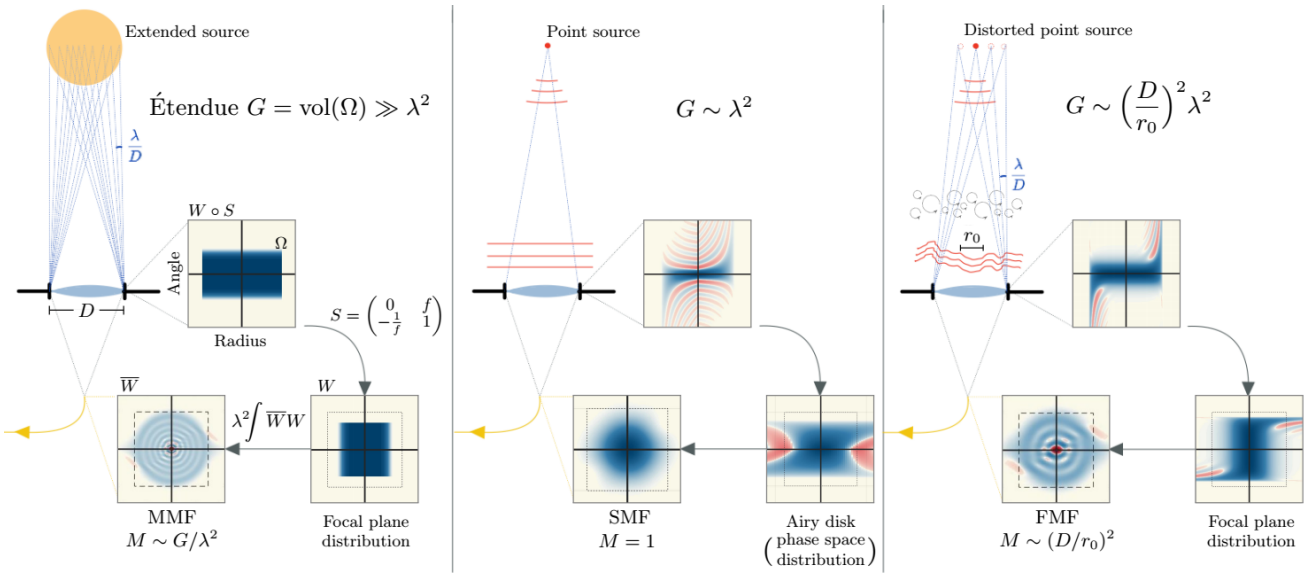

Figure 1. Schematic for a phase space representation of a range of fiber-coupled free-space optical systems from highly multi-mode systems to single-mode diffraction-limited systems. The Wigner phase space distribution function is used to study the transition from single-mode to multi-mode systems. Wigner functions typical of each scenario are illustrated via the polar phase space diagrams discussed in Section 3.1.

marginal given by the Airy pattern. This diffraction-limited quasi-distribution exhibits the negative values typical of non-Gaussian coherent optical fields. The Wigner distribution associated to the fundamental mode of the fiber is very similar to that of a Gaussian beam (see also Figure 3).

The case of primary interest in this work is illustrated in the third panel of Figure 1. Here, incident light arriving from an atmospherically distorted beam has a hard cut-off at the pupil radius q but exhibits an angular spread which includes both coherent effects from diffraction at the pupil as well as a statistical spread in propagation angle over the aperture due to atmospheric phase perturbations. As the number of guided modes in the fiber increases, coupling to the fiber transitions from a strong dependence on mode-matching to a more general dependence on the geometrical phase space acceptance of the waveguide Wigner distribution (Sec. 3.1 and 3.4).

3.1 Waveguide Wigner distributions

In this Section we analyze the waveguide distributions for a collection of step-index and graded-index fibers, as well as the distributions associated to guided modes at the insertion (fused) end of several photonic lantern structures listed in Table 1. A parabolic index profile is assumed within the core of the graded-index fibers characterized by the nominal numerical aperture $\mathrm{NA}_w = (n_1^2 - n_2^2)^{1/2}$ where n_1 is the on-axis core refractive index and n_2 is the cladding index. The photonic lantern structures studied model insertion directly into the fused end of a 1×7 lantern with refractive index profile characterized by a residual core radius, residual cladding radius, and fused core radius, as shown in Figure 2.[26] For the 7-mode lantern we assume constant indices in the residual core and fused core. The 42-mode structure models an idealized version of a 42-mode FMF lantern based on the description in Ref. 3 with a parabolic index within the residual cores and constant index within the fused core.

The guided modes were calculated using a finite-difference method to solve the scalar Helmholtz equation

$$\left(\nabla^2 + k_0^2 n^2(\vec{x})\right) \psi = 0$$

and are normalized so that $|\langle \psi, \psi \rangle|^2 = 1$. The Wigner distributions were calculated using the discrete Wigner transform by down-sampling the modes from the finite-difference grid to a 512×512 DFT grid optimized for the discrete Wigner transform following the procedure described in Appendix A.

#Guided modes (per pol.)		1	3	6	7	10	15	21	30	36	42	51	55	78
Core radius a_w [μm]	Step-index (SI)	2.95	4.5	6	-	7.5	9	10.75	13.5	14.5	-	17.5	18	21.5
	Graded-index (GI)	4	6	9	-	11	13	15	19.25	21	-	24.5	26	30
Residual core radius [μm]	Photonic lantern (PL)	-	-	-	0.669	-	-	-	-	-	1.31	-	-	-
Residual clad. radius [μm]		-	-	-	8.24	-	-	-	-	-	8.25	-	-	-
Fused core radius [μm]		-	-	-	23.1	-	-	-	-	-	23	-	-	-
Numerical aperture NA_w	Step-index (SI) / Graded-index (GI)	0.2												
Residual core NA	Photonic lantern (PL)	-	-	-	0.17	-	-	-	-	-	0.121	-	-	-
Fused core NA		-	-	-	0.051	-	-	-	-	-	0.131	-	-	-

Table 1. Listing of parameters characterizing waveguide refractive index profiles for waveguide structures studied below with guided modes calculated assuming a vacuum wavelength $\lambda = 1.55$ μm.

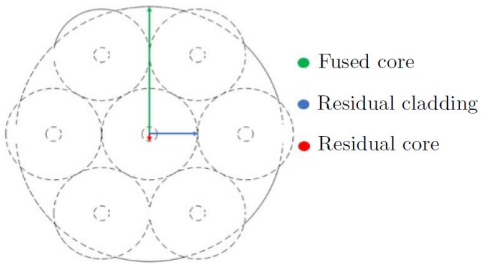

Figure 2. Schematic diagram of the fused end of the photonic lantern structure.

The discrete Wigner distribution can be inspected via a phase space diagram (PSD) as shown in Figure 3 for a 3-mode graded-index fiber. In contrast to the PSDs for 1D signals used in time-frequency analysis, the PSD for a 2D optical signal is necessarily limited since one cannot plot the Wigner distribution on the full 4-dimensional phase space domain. In Figure 3 we plot a partial PSD using polar coordinates $\vec{q} = (q\cos\theta, q\sin\theta)$ and $\vec{p} = (p\cos\phi, p\sin\phi)$. In each quadrant we fix the angles θ, ϕ and plot the Wigner function in terms of the radius $q = |\vec{q}|$ and angular radius $p = |\vec{p}|$. This four-quadrant polar PSD captures much of the mode structure for modes ψ with axial symmetry since W_ψ depends only on the difference $\phi - \theta$.

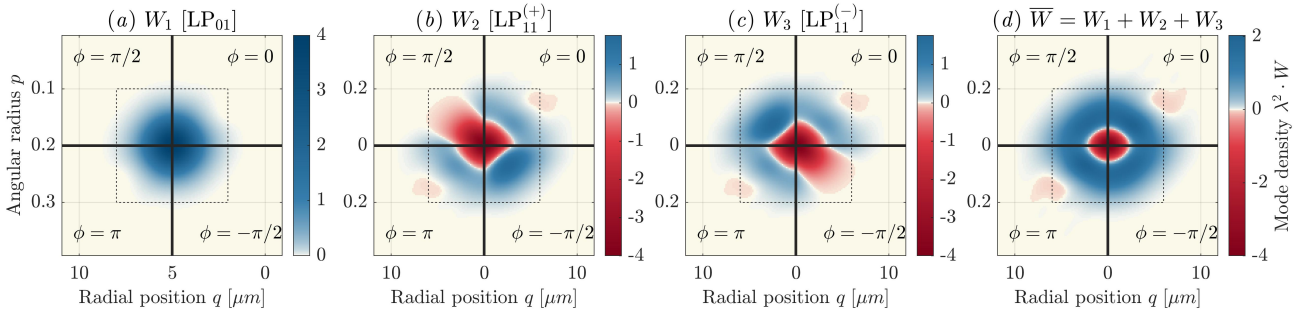

Figure 3. Polar phase space diagram for the guided modes in a 3-mode graded-index fiber with $\theta = 0$. The polar PSD for the waveguide distribution $\overline{W} = W_1 + W_2 + W_3$ is shown on the right. The dashed overlay shows the core radius and numerical aperture. Quadrants 2 and 4 (where $\vec{p}$ is oriented at a right angle to $\vec{q}$) serve to distinguish the orientation of the orbital angular momentum (OAM) modes $\mathrm{LP}_{11}^{(\pm)} = \sqrt{1/2}(\mathrm{LP}_{11}^{(e)} \pm i\mathrm{LP}_{11}^{(o)})$. The normalized value of the Wigner function is described as a differential mode density following the discussion at the end of Section 3.1.

In addition to verifying sufficient sampling, the polar PSD can be useful for gaining insight into the nature of the light propagating in the waveguide. In Figure 4 we have plotted the waveguide distributions for a number of

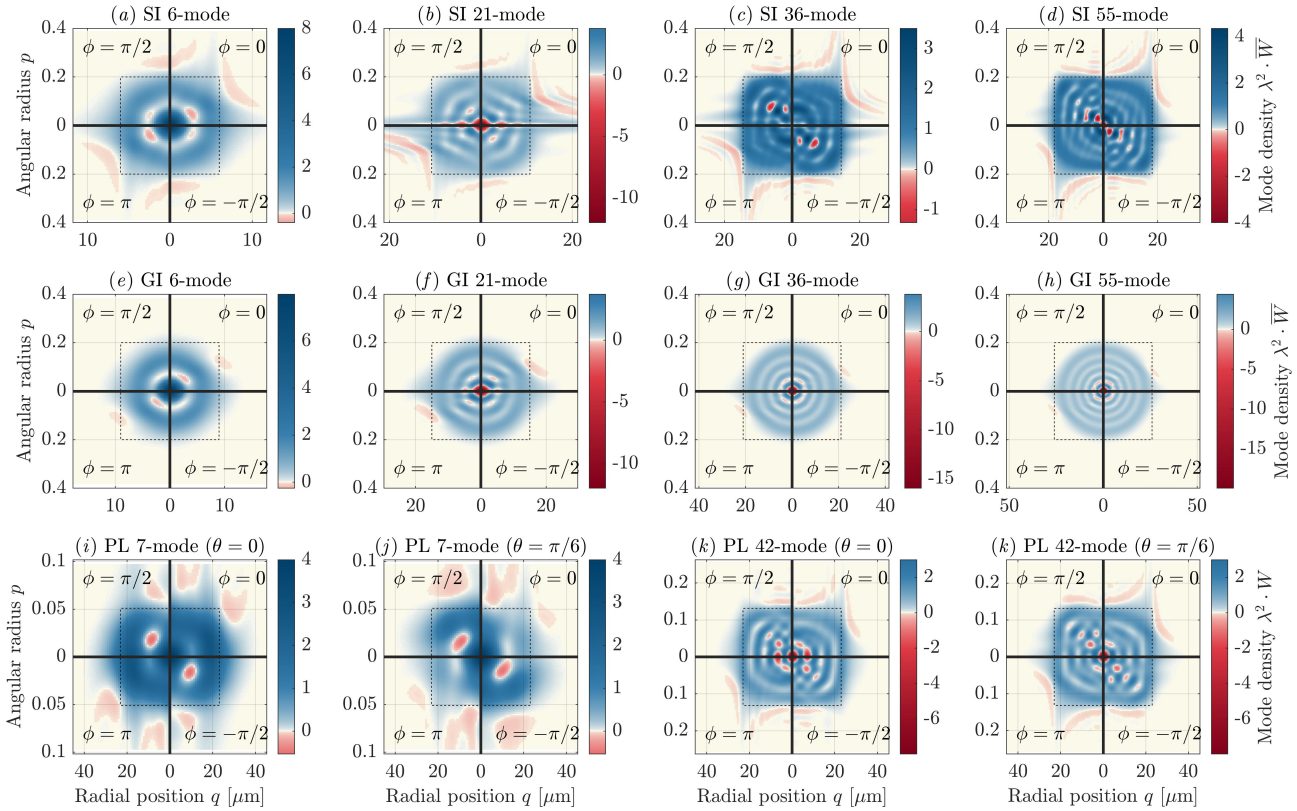

Figure 4. Polar PSDs for waveguide distributions for step-index fibers (first row) and parabolic-index fibers (second row). The bottom row shows PSDs for photonic lantern structures with 7 modes and 42 modes along the radial vectors $\theta = 0$ and $\theta = \pi/6$. The dashed overlay shows the core radius and NA (the fused core NA is shown for the photonic lanterns).

step-index and graded-index fibers, as well as for the guided modes carried at the insertion end of the photonic lantern structures. The step-index fibers are generally well-confined within the phase-space domain defined by the core radius $q < a_w$ and numerical aperture $p < \mathrm{NA}_w$, although the presence of modes which extend into the cladding can be seen particularly when there are guided modes close to cutoff (e.g. in the 21 mode step-index fiber in the top row). This confinement is also seen in the parabolic-index fibers, except that the support of the waveguide distributions for these fibers is better described by the 4-dimensional ellipsoid $(q/a_w)^2+(p/\mathrm{NA}_w)^2 < 1$. This observation motivates a geometrical optics waveguide approximation for parabolic-index fibers given by

$$\overline{W}_{pi}(\vec{q},\vec{p}) = \begin{cases} 1/\lambda^2 & (q/q_w)^2 + (p/p_w)^2 < 1 \\ 0 & \text{otherwise,} \end{cases} \qquad \text{(parabolic-index approximation)} \tag{9}$$

which is analogous to the geometrical optics waveguide approximation for step-index fibers used in Ref. 15

$$\overline{W}_{si}(\vec{q},\vec{p}) = \begin{cases} 1/\lambda^2 & q < q_w \text{ and } p < p_w \\ 0 & \text{otherwise,} \end{cases} \qquad \text{(step-index approximation).} \tag{10}$$

Just as the condition $\int \overline{W}_{si} = M$ can be enforced by requiring $\pi^2 q_w^2 p_w^2 = M\lambda^2$, the condition $\int \overline{W}_{pi} = M$ requires $2\pi^2 q_w^2 p_w^2 = M\lambda^2$. Note that both agree with the usual estimates for the number of modes (per polarization) in a step-index fiber $M \simeq V^2/4$ and graded-index fiber $M \simeq V^2/8$ if one takes q_w and p_w as the core radius and NA, respectively. In analogy with the phase space acceptance of an optical mode,[27] we shall refer to the domains defined by (9)-(10), with $q_w = a_w$ and $p_w = \mathrm{NA}_w$, as the geometrical phase space acceptance (or simply as the geometrical acceptance) of the respective waveguides.

In contrast to the waveguide distributions for step-index and parabolic-index fibers, the waveguide distributions for the fused photonic lantern structures do not have continuous axial symmetry, but do exhibit a six-fold rotational symmetry. Figure 4 shows the waveguide distributions along the radial vector $\theta = 0$ which passes through one of the residual cores, and along a vector $\theta = \pi/6$ which passes between two residual cores (see Figure 2). The presence of higher NA residual cores can be seen in the 7-mode lantern through the increased angular spread at $q = 0$ and $q = 16$ μm when $\theta = 0$. The presence of the residual cores is not visible in the 42-mode structure where the NA of the residual cores is less than that of the fused core. Since the insertion efficiency is generally maximized by taking the the NA of the focusing system close to the NA of the fused core (*cf.* Sec. 3.4), one can expect modes with significant intensity in higher NA residual cores to be less effective for coupling light arriving from a telescope. However, as the area of the residual cores is generally small relative to that of the fused core, one can expect this inefficiency to be small.

This situation can be quantified by calculating a mode density

$$\delta(\Omega) = \frac{\lambda^2}{\mathrm{vol}(\Omega)} \int_\Omega \overline{W}\; d^2\vec{q} d^2\vec{p}$$

associated to a phase space domain Ω. For larger domains $G \equiv \mathrm{vol}(\Omega) \gg \lambda^2$ this represents the maximum efficiency with which incoherent light can be coupled to the fiber from an optical system with étendue G arranged to deliver light into the domain Ω at the fiber entrance plane. This interpretation breaks down for domains with smaller étendue $G \sim \lambda^2$ which do not support incoherent light and must be replaced by the more general understanding that the coupling efficiency is typically improved when light can be delivered into a domain Ω in which $\overline{W}$ has a high mode density. Table 2 shows a numerical calculation of the mode density of the waveguides described in Table 1 with respect to the geometrical phase space acceptance using (9) for the graded-index fibers and the step-index acceptance (10) for the photonic lanterns.

#Guided modes		1	3	6	7	10	15	21	30	36	42	51	55	78
Mode density within geometrical acceptance	SI	0.55	0.71	0.8	-	0.88	0.88	0.89	0.88	0.91	-	0.91	0.93	0.93
	GI	0.63	0.84	0.81	-	0.89	0.94	0.98	0.89	0.92	-	0.94	0.93	0.97
	PL	-	-	-	0.92	-	-	-	-	-	0.94	-	-	-

Table 2. Mode density for a selection of step-index, graded-index, and photonic lantern structures with respect to the geometrical phase space acceptance. The step-index acceptance (10) is used for the photonic lantern with respect to the fused core radius.

Note that the mode density within the geometrical phase space acceptance generally increases with the number of modes. Although the step-index acceptance for a fiber with M guided modes generally has the same volume $M\lambda^2$ as the parabolic-index acceptance, the mode density for the graded-index fibers is slightly higher. However, to take advantage of this one would need an optical system designed to deliver light into the ellipsoidal parabolic-index acceptance which simple focusing systems do not accomplish (*cf.* Section 3.4). To estimate the impact of the higher NA residual cores in the photonic lanterns, the residual core NA was reduced to the fused core NA while simultaneously increasing the residual core radius to maintain the same number of supported modes. For the 7-mode structure in Table 1, the mode density increased less than 0.005 owing to the small area of the residual cores.

By considering an appropriate sequence of shrinking domains one obtains in the limit $\delta(\Omega) \to \lambda^2 \overline{W}$. This gives an interpretation of the quantity presented in Figures 3 and 4 as a differential mode density. This interpretation comes with the caveat that such a quantity has no physical meaning for domains which violate the optical uncertainty relation $\Delta q_x \Delta q_y \Delta p_x \Delta p_y \geq \lambda^2/(4\pi)^2$ and so should only be considered as such when integrated over an appropriate domain.

3.2 Atmospheric long and short exposure Wigner distributions

The Wigner distribution associated to a plane wave in a circular aperture after propagation through atmospheric turbulence can be calculated based on the MCF of the incident optical field. Based on the analysis of Fried and

Heidbreder,[28,29] one can derive two distinct MCFs associated to long-exposure and short-exposure statistics, respectively. The Wigner distribution associated to long-exposure statistics was studied in detail in Ref. 15. The short-exposure statistics assume the tilt of the arriving wavefront is removed, commonly accomplished by splitting off some of the light to perform active tilt compensation using a fast steering mirror. It should be noted that these models assume homogeneous and isotropic Kolmogorov turbulence with negligible scintillation across the aperture and ignore the effects of a finite outer scale. The long-exposure MCF in an aperture with pupil function $P(\vec{x})$ is given by

$$\mu_{\vec{q}}(\vec{r}) = \frac{1}{\mathcal{A}} \exp\left[-3.44\Big(\frac{r}{r_0}\Big)^{5/3}\right] P(\vec{q}+\vec{r}/2)P(\vec{q}-\vec{r}/2)$$

where $r = |\vec{r}|$, r_0 is the atmospheric coherence diameter, and $\mathcal{A}$ is the area of the pupil. The short-exposure MCF for a circular pupil of diameter D takes the form

$$\mu_{\vec{q}}(\vec{r}) = \frac{4}{\pi D^2} \exp\left[-3.44\Big(\frac{r}{r_0}\Big)^{5/3} - 32\pi^2\langle\tau_x^2\rangle\Big(\frac{r}{D}\Big)^2 + \mathcal{C}_{\vec{q}}(\vec{r})\right] \Theta(D-|2\vec{q}+\vec{r}|)\Theta(D-|2\vec{q}-\vec{r}|)$$

where $\langle\tau_x^2\rangle$ is the mean square Zernike tilt along a fixed axis and $\mathcal{C}_{\vec{q}}(\vec{r})$ is the covariance of the tilt-phase and the total phase[29]

$$\langle\tau_x^2\rangle = \frac{2^{1/3}}{32\pi^2} \cdot 0.8281 \cdot 6.88\Big(\frac{D}{r_0}\Big)^{5/3} \tag{11}$$

$$\mathcal{C}_{\vec{q}}(\vec{r}) = \frac{2^{1/3}}{\pi} \cdot 6.88\Big(\frac{D}{r_0}\Big)^{5/3} \iint_{|\vec{u}|\leq 1} \vec{u}\cdot\frac{\vec{r}}{D}\Big(\Big|\vec{u}-\frac{2\vec{q}-\vec{r}}{D}\Big|^{5/3} - \Big|\vec{u}-\frac{2\vec{q}+\vec{r}}{D}\Big|^{5/3}\Big) d^2\vec{u}. \tag{12}$$

Note that the integral above is a purely geometric quantity depending only on the normalized position $\vec{q}/(D/2)$ and separation $\vec{r}/D$ within the aperture. The MCFs were sampled on a DFT grid of size 2048×2048 with sample spacing $\Delta r = 2\Delta q$ chosen to obtain equal sampling $q_0/\Delta q = p_0/\Delta p$ within the characteristic scales $q_0 = D/2$ and $p_0 = (\lambda/D)\sqrt{16+(D/r_0)^2}$. Polar PSDs of the associated long-exposure and short-exposure Wigner distributions are shown in Figure 5.

For $D/r_0 = 2$ (not shown) the phase perturbation is dominated by tilt and so the short-exposure Wigner distribution still resembles the diffraction-limited distribution for a circular aperture, although the 80% encircled energy radius is pushed to the second lobe of the Airy-like pattern. Note that for severe turbulence conditions $D/r_0 \sim 20$ the short-exposure distribution is at least coarsely similar to the long-exposure distribution with a smaller angular spread; however, in moderate conditions $D/r_0 \lesssim 10$ the effect of tilt removal is more subtle. The reduction in the width of the distribution for a given enclosed energy is shown in Figure 6.

Figure 5 also shows the PSD for a circular aperture with a circular central obscuration with obscuration diameter ratio $\varepsilon = 0.27$ (bottom row). For diffraction-limited coupling ($D/r_0 = 0$) the obscuration introduces interference effects in the central portion of the Wigner distribution $q < \varepsilon D/2$ even though there is no light in this region (i.e. the spatial marginal vanishes for $q < \varepsilon D/2$). With 27% linear obscuration ratio the 80% encircled energy radius is nearly doubled in the diffraction limit. However at higher D/r_0 coherent diffraction effects appear only within a distance r_0 from the boundary of the pupil. As a result, at higher turbulence levels the Wigner distribution vanishes up to the obscured radius $\varepsilon D/2$ and exhibits only a minor increase to the encircled energy radii which are dominated by the dependence on the seeing parameter λ/r_0.

3.3 Coupling efficiency

The primary limitation of using the PSF and encircled energy alone to analyze coupling to few-mode fibers is the fact that the optical field overlap integrals are based on the complex field and the intensity PSF gives little insight into the nature of the dependence of the coupling on the numerical aperture of the focusing system. In this section we study this dependence in various atmospheric conditions using the phase space distributions discussed in the previous sections.

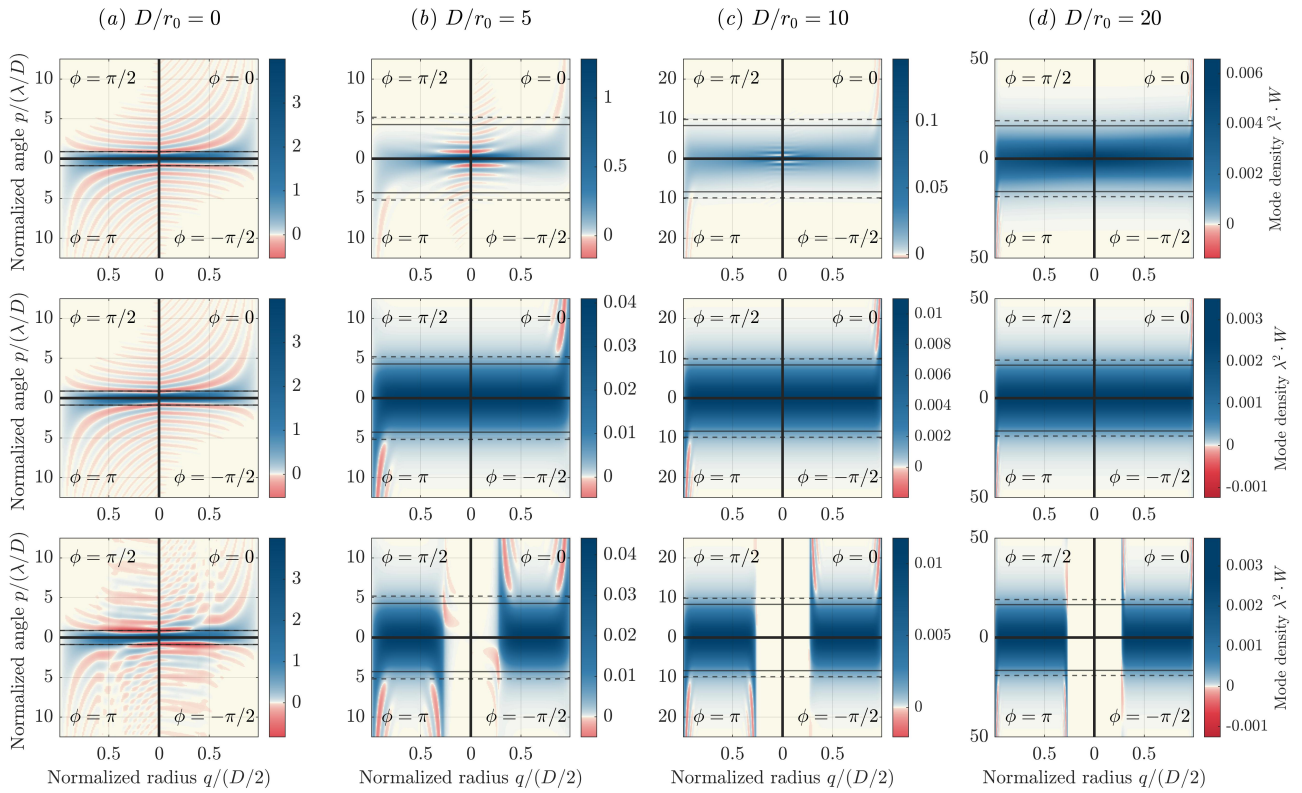

Figure 5. Polar PSDs for short-exposure Wigner distribution (top row), long-exposure Wigner distribution (middle row), and centrally obscured ($\varepsilon = 0.27$) long-exposure Wigner distribution (bottom row) with $D/r_0 = 0, 5, 10$, and 20. Horizontal lines show the angular radii containing 80% encircled energy in the long- and short-exposure distributions.

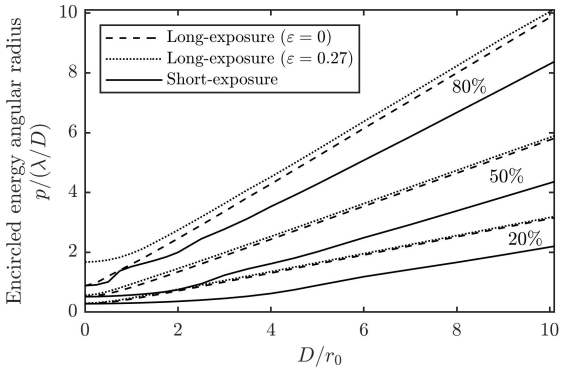

Figure 6. Angular radii containing 80%, 50%, and 20% encircled energy in units of λ/D.

Assuming a simple focusing system with numerical aperture $\mathrm{NA}_f = D/2f$ is employed to couple light from a telescope to an optical fiber, the evolution of the Wigner distribution from the aperture plane to the fiber entrance plane is modeled by the transfer matrix

$$A = \begin{pmatrix} 1 & 0 & 0 & 0 & \Delta q_x \\ 0 & 1 & 0 & 0 & \Delta q_y \\ 0 & 0 & 1 & 0 & \Delta p_x \\ 0 & 0 & 0 & 1 & \Delta p_y \\ 0 & 0 & 0 & 0 & 1 \end{pmatrix} B \begin{pmatrix} 0 & 0 & f & 0 & 0 \\ 0 & 0 & 0 & f & 0 \\ -1/f & 0 & 1 & 0 & 0 \\ 0 & -1/f & 0 & 1 & 0 \\ 0 & 0 & 0 & 0 & 1 \end{pmatrix} \tag{13}$$

where $\Delta\vec{q}$ and $\Delta\vec{p}$ represent misalignments of the fiber in the focal plane via a transverse displacement and tilt,

respectively, and B is a defocusing matrix representing displacement of the fiber along the optical axis. For the results presented in this work, we assume perfect alignment $\Delta\vec{q} = \Delta\vec{p} = 0$ and $B = I$. Since the long- and short-exposure Wigner distributions depend only on the ratio D/r_0, we may work with distributions normalized to a unit radius aperture, and the above reduces to a dependence on the numerical aperture $\mathrm{NA}_f \equiv D/2f = 1/f$.

The optimal efficiency and input NA can be found by sweeping over the focal length f. An analysis of the optimal efficiency for step-index fibers based on long-exposure statistics was given in Ref. 15 yielding an approximation

$$\eta_{si} \simeq \Sigma^4/M^8 + 0.822[1 - e^{-3\cdot\Sigma^2}] + 0.103[1 - \Gamma(4, 3\cdot\Sigma^2)/3!)] + 0.028[1 - \Gamma(10, 3\cdot\Sigma^2)/9!] \tag{14}$$

depending on a single efficiency parameter $\Sigma^2 = (4/\pi^2)M\mathcal{S}_{LE}$ where $\mathcal{S}_{LE} = (1 + (D/r_0)^{5/3})^{-6/5}$ is an approximation to the long-exposure Strehl ratio and $\Gamma(s, x)$ is the upper incomplete gamma function. The correction term Σ^4/M^8 accounts for the anomalous behavior of the SMF seen in Figure 7. Although (14) was derived based

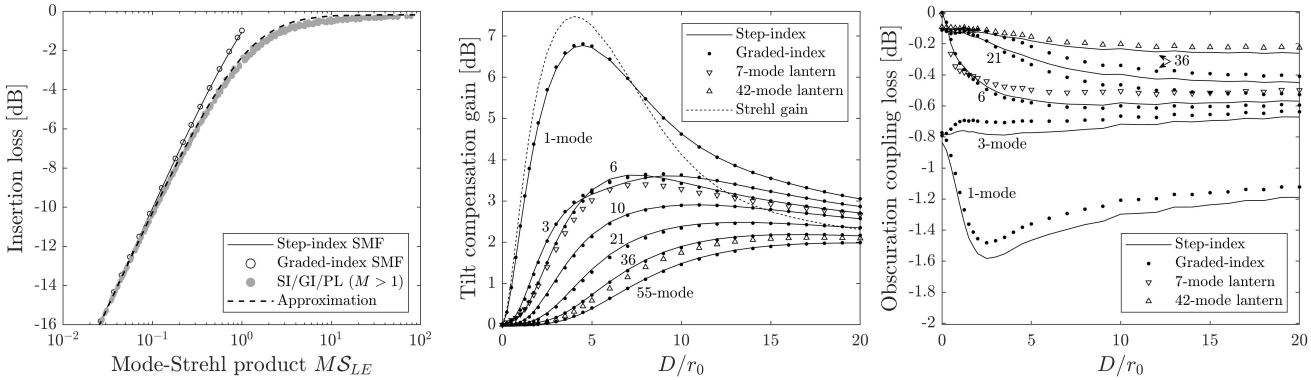

Figure 7. Insertion loss based on long-exposure Wigner distribution in a circular aperture for all fibers in Table 1 (left). Comparison of gain from tilt compensation for several step-index, graded-index, and photonic lantern structures (center). Coupling loss due to central obscuration ($\varepsilon = 0.27$) using long-exposure Wigner distribution (right).

on an analysis of step-index fibers we find that for the range of fibers in Table 1 the optimal efficiency for the step-index fibers and graded-index fibers with the same number of modes agree within 0.13 dB for both long- and short-exposure statistics in an unobscured circular aperture. The optimal insertion efficiency for all fibers in Table 1 obeys the same general dependence on M and D/r_0 shown in Figure 7 and agrees with (14) within 0.4 dB. It should be emphasized that the insertion loss relates only to injection into the fiber and does not include propagation losses including those incurred in the tapered photonic lantern transition.

On the other hand, the optimal efficiency and coupling geometry in the presence of a central obscuration exhibits subtle differences based on the geometry of the spatial modes of the waveguide (right side of Figure 7). This is illustrated in Figure 8, where the geometrical acceptance of the 21-mode fibers has been overlaid on the PSDs of the incident light propagated to the focal plane. The propagation was done using the optimal input NA for the 21-mode graded-index fiber. There is a significant reduction in coupling loss for fibers which support modes LP_{lm} of radial order at least $m \geq 2$. This can be attributed to the second lobe of the waveguide distributions seen in Figure 4 better matching the bias towards higher angle light coming from the annular aperture (bottom row of Figure 8). This can be seen in the natural overlap of the second lobe with the obscured long-exposure Wigner distribution.

Note that the ring structure in the 3-mode waveguide distribution provides a similar benefit via an improved overlap at higher turbulence levels, but under-performs in the diffraction limit due to interference effects in the center of the obscured Wigner distribution (compare Figure 3 and bottom left of Figure 8). At higher turbulence levels the obscuration-induced coupling loss for step- and graded-index fibers differs (within 0.2 dB) for fibers which support more than ∼10-20 modes. This appears to be due to the fact that as the number of modes increases the step-index waveguide distrubutions begin to approach the step-index acceptance (quantified by the mode density in Table 2). The step-index acceptance yields better overlap with the obscured long-exposure

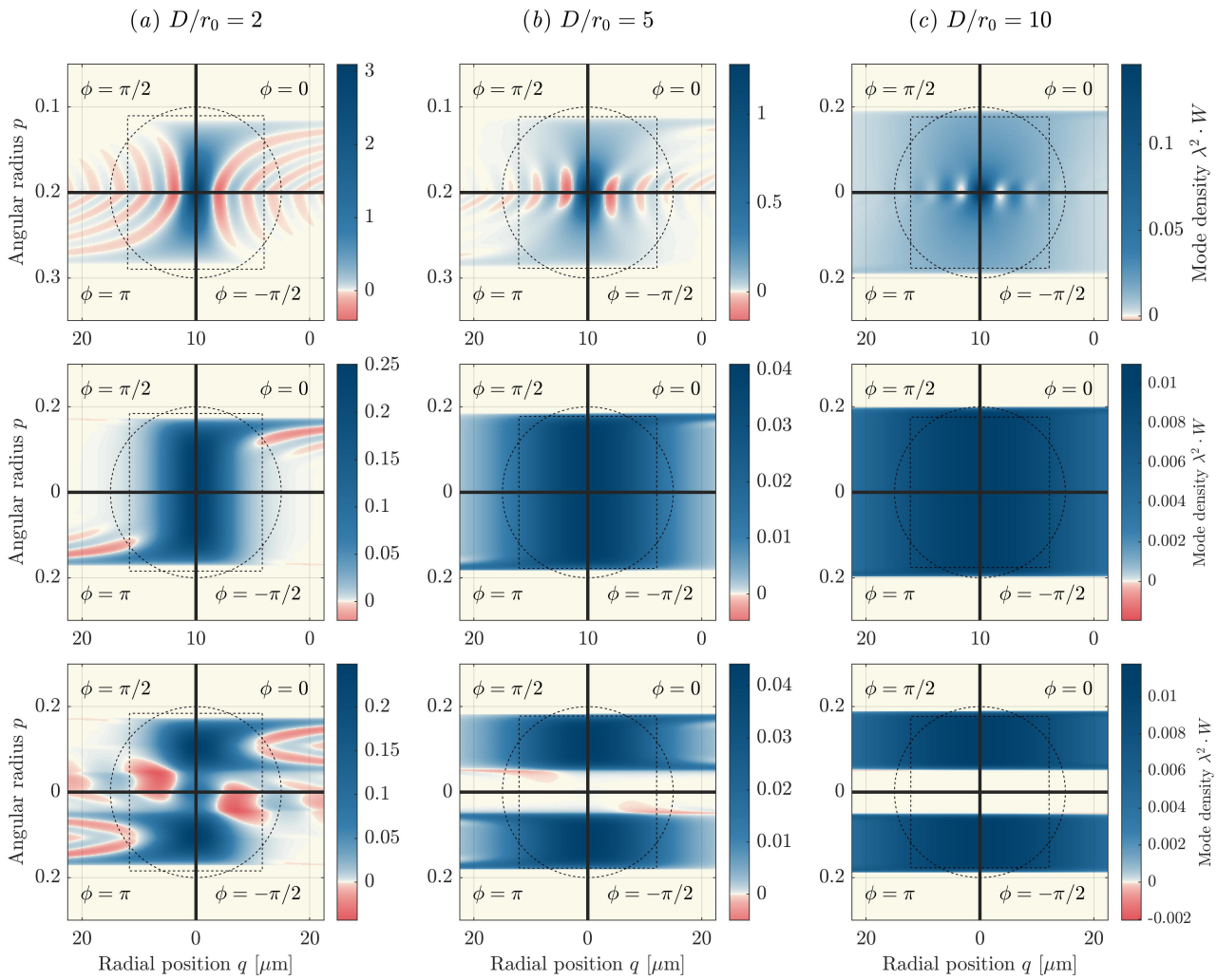

Figure 8. Polar PSDs showing the geometrical acceptance for a 21-mode graded-index fiber (dashed circle) and step-index fiber (dashed rectangle) against the short-exposure Wigner function (top row), long-exposure Wigner function (middle row), and long-exposure Wigner function with central obscuration $\varepsilon = 0.27$ (bottom row). Three turbulence conditions are shown with $D/r_0 = 2, 5$, and 10. The edge of the horizontal band identifies the NA of the focusing system. The atmospheric Wigner functions have been propagated to the focal plane using the optimal f-number for the graded-index fiber. The optimal NA for the step-index fiber is shown on the same plot by rescaling the geometrical acceptance (i.e. by inversely scaling the NA and core diameter of the step-index fiber).

Wigner distribution due to the bias of the parabolic-index acceptance for low-angle light (bottom row of Figure 8). The obscuration-induced insertion loss for the photonic lanterns roughly tracks that of the step-index fibers with a similar mode-count.

3.4 Optimal NA and tolerance

In Figure 9, a calculation of the optimal input NA is shown for the fibers in Table 1 in a range of conditions with $D/r_0 \leq 20$. The bars above and below each data point denote the NA range corresponding to a 0.1 dB drop in efficiency on either side of the optimum. The data for the photonic lanterns is normalized by the fused core NA.

Except for several few-mode fibers with less than 10 modes, the optimal NA for a given index profile depends primarily on the ratio $(D/r_0)/\sqrt{M}$. This parameter expresses the general efficiency regime through Eq. (14). The optimal NA for the photonic lanterns exhibits roughly the same behavior as the step-index fibers, though it

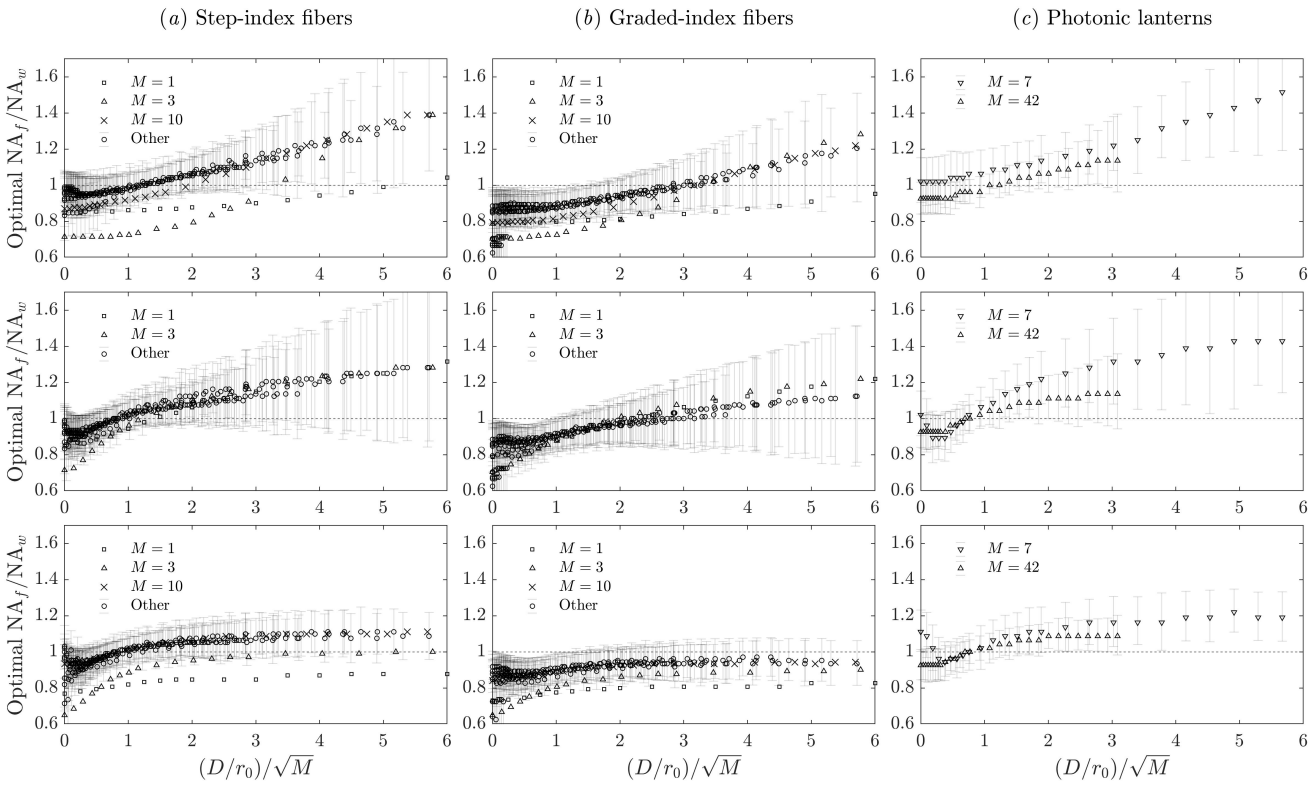

Figure 9. Optimal input NA for optical fibers in Table 1 with increasing turbulence using the short-exposure Wigner function (top row), long-exposure Wigner function (middle row) and long-exposure Wigner function with central obscuration $\varepsilon = 0.27$ (bottom row). The bars show the 0.1 dB tolerance for each fiber (tolerances have been omitted from the anomalous few-mode fibers in the legend to make the general trend visible).

should again be stated that this only reflects the insertion coupling. Propagation through the tapered transition of the lantern may have an effect on the optimal NA which is not modeled here.

For the graded-index fibers near the diffraction-limit, we observe the well-known behavior whereby the graded-index fibers are typically optimized with the input NA slightly below the nominal NA of the parabolic-index fiber. In terms of the Wigner distributions, this can be interpreted via the PSDs exhibiting the optimal NA ratio shown in Figure 8. In the focal plane, the Wigner distribution of the incident light exhibits a hard cutoff at the NA of the focusing system (i.e. at the angular radius corresponding to the pupil boundary). In order to collect the large amount of light from the edge of the aperture (the top and bottom edges of the horizontal bands in Figure 7) the NA of the parabolic-index fiber is optimized slightly above that of the focusing system so that the light near the edge of the aperture is well-contained within the geometrical acceptance of the fiber.

Figure 9 also shows that the optimal input NA with unobscured apertures (top two rows) increases as the turbulence increases. In the low-efficiency regime $D/r_0 > 2\sqrt{M}$, the light becomes uniformly spread both in position and propagation angle over the face of the fiber (right side of Figure 8). Under these conditions efficiency is maximized by ensuring the light overfills the geometrical acceptance of the fiber. Although the optimum in this regime typically occurs with the input NA larger than that of the fiber, the tolerance is large since very little light is coupled at angles larger than the geometrical acceptance allows (*cf.* Figure 4).

The optimal input NA does not continue to increase with increasing turbulence for obscured apertures (bottom row of Figure 9). In severe turbulence, the vanishing of the distribution at low propagation angle stops the continuous increase in the optimum input NA to ensure that the system delivers as much light as possible from the outer portion of the annular pupil into the geometrical acceptance of the fiber (bottom row of Figure 8). As the light becomes less coherent this results in a strict balance between the input NA and waveguide NA which

depends on the shape of the geometrical acceptance of the waveguide. The need to accommodate this balance results in the smaller tolerance in the NA for simple focusing systems (13) with centrally obscured pupils.

It should be noted that these observations hold only for simple focusing systems described by (13). More sophisticated passive techniques such as apodization— including low-loss phase-induced amplitude apodization (PIAA)[30]—can improve the delivery of light into the geometrical acceptance of the waveguide by considering more general optical transformations than those described by (13). Such systems can be designed to change the coupling geometry and improve efficiency in the presence of obscurations.[6]

4. CONCLUSIONS

A numerical method based on phase space representations was outlined to study coupling from a telescope to an optical fiber for free-space optical systems. The dependence of the coupling geometry on the mode structure of the waveguide was analyzed for optical receiver systems operating in various atmospheric conditions with and without tilt compensation. In the absence of obscurations, the optimal coupling efficiency was found to be largely independent of mode structure depending only on the number of guided modes M (Figure 7). For fibers with more than 6-10 guided modes, the optimal coupling geometry was found to be dependent primarily on the geometrical phase space acceptance and the efficiency regime characterized by the ratio $(D/r_0)/\sqrt{M}$ (Figure 9). A general analysis of the coupling geometry was found to break down for fibers with less than 10 guided modes. This suggests a fiber-specific system analysis is especially advisable for receivers coupling to fibers with less than 10 guided modes.

In the presence of a central obscuration in the telescope, the efficiency was shown to have a dependence on the mode structure and geometrical acceptance of the fiber (Figure 7). The optimal NA at increasing turbulence levels was found to limit to a strict balance between the NA of the focusing system and waveguide with a tighter tolerance than for the unobscured aperture (Figure 9). Phase space diagrams were employed to interpret numerical results and provided a robust method for analyzing optical systems in the transition from single-mode to multi-mode behavior within a wave-optical framework.

APPENDIX A. SAMPLING FOR THE DISCRETE WIGNER TRANSFORM

One of the fundamental properties of the version of the discrete Wigner transform described in Section 2.1 is that the sampling of the Wigner transform in the space and frequency domains are coupled through the DFT. For a signal $\psi(\vec{x})$ sampled on an $N \times N$ grid $\psi_{ij} = \psi(x_i, x_j)$ with spacing Δx, the Wigner transform is sampled on a grid (x_i, x_j, ξ_k, ξ_l) with

$$\Delta x \Delta \xi = \frac{1}{2N}.$$

The choice of the sample size N thus amounts to a choice of the volume of the discretized phase space element. The only way to obtain finer sampling of the Wigner transform in both domains is to increase the DFT size N.

Due to the trade between resolution in space and frequency domains for a fixed DFT size, the spacing Δx can be chosen to balance the sampling in both domains by fixing the ratio

$$\frac{\Delta x}{\Delta \xi} = 2N\Delta x^2 \equiv \ell^2 \tag{15}$$

where ℓ has the dimensions of length for a spatial signal and can be understood as a spatial scale which is sampled equally in the space and frequency domains $\ell/\Delta x = \xi_\ell/\Delta\xi$ where $\xi_\ell = 1/\ell$. In practice, the characteristic scale can be chosen by determining a pair of scales x_0 and ξ_0 to be sampled equally. This is enforced by taking $\ell = \sqrt{x_0/\xi_0}$—the geometric mean of the length x_0 and spatial period $1/\xi_0$—and choosing Δx based on N and ℓ through (15).

Another consequence of the DFT-based method is that oversampling a signal with width w and bandwidth b relative to the minimal requirement $N\Delta x \geq w$ and $N\Delta\xi \geq b$ is inextricably coupled to an increase in the volume of the phase space domain sampled by the DWT which is proportional to

$$(N\Delta x)(N\Delta\xi) = \frac{N}{2}.$$

To improve interpolation it is generally beneficial to oversample the transform within the region of interest characterized by w and b; however, the resulting increase in sampling outside this region of interest yields little additional information needed to analyze the signal. In addition to the $O(N^4)$ memory requirement, a large sampling grid can lead to significant computation time of subsequent operations on the Wigner distribution including interpolation and inner products (Sec. 2.3). Subsequent operations can be made more efficient by truncating the full discrete Wigner transform to the region of interest with

$$N_w = \sqrt{2N}\frac{w}{\ell}, \qquad N_b = \sqrt{2N}\ell b. \tag{16}$$

Restricting the calculation to this domain reduces the number of DFTs from N^2 to N_w^2 and one can truncate the DFT from a frequency-domain grid of size N^2 to a grid of size N_b^2. Observe that the total memory requirement is independent of ℓ and is given by

$$N_w^2 N_b^2 = 4N^2(wb)^2.$$

The memory requirement is thus determined by the dimensionless space-bandwidth product of the signal (e.g. for modes in an optical fiber this is determined by the V-number). The choice of the characteristic length ℓ thus amounts to a splitting of this memory into sampling in the space or frequency domain. The $O(N^2w^2b^2)$ memory requirement can be further reduced for signals and optical modes which exhibit symmetry. For example, with full axial symmetry the memory requirement can be reduced by a factor N_w to $O(N^2(w\Delta x)^2b^2)$.

ACKNOWLEDGMENTS

This work is supported by the NASA Space Communications and Navigation (SCaN) Program and the Glenn Research Center Communications & Intelligent Systems Division.

REFERENCES

[1] Wright, M. W., Morris, J. F., Kovalik, J. M., Andrews, K. S., Abrahamson, M. J., and Biswas, A., "Adaptive optics correction into single mode fiber for a low earth orbiting space to ground optical communication link using the opals downlink," *Opt. Express* **23**, 33705–33712 (Dec 2015).

[2] Vyhnalek, B. E., Nappier, J. M., and Tedder, S. A., "Real time photon-counting receiver for high photon efficiency optical communications," in [*2019 IEEE International Conference on Space Optical Systems and Applications (ICSOS)*], 1–6 (2019).

[3] Tedder, S. A., Floyd, B., Chahine, Y. K., Croop, B., Vyhnalek, B. E., Betters, C., and Leon-Saval, S. G., "Measurements of few-mode fiber photonic lanterns in emulated atmospheric conditions for a low earth orbit space to ground optical communication receiver application," in [*Free-Space Laser Communications XXXII*], Hemmati, H. and Boroson, D. M., eds., **11272**, 183 – 192, International Society for Optics and Photonics, SPIE (2020).

[4] Wagner, R. E. and Tomlinson, W. J., "Coupling efficiency of optics in single-mode fiber components," *Appl. Opt.* **21**, 2671–2688 (Aug 1982).

[5] Shaklan, S. and Roddier, F., "Coupling starlight into single-mode fiber optics," *Appl. Opt.* **27**, 2334–2338 (Jun 1988).

[6] Jovanovic, N., Schwab, C., Guyon, O., Lozi, J., Cvetojevic, N., Martinache, F., Leon-Saval, S., Norris, B., Gross, S., Doughty, D., Currie, T., and Takato, N., "Efficient injection from large telescopes into single-mode fibres: Enabling the era of ultra-precision astronomy," *A & A* **604**, A122 (2017).

[7] Horton, A. J. and Bland-Hawthorn, J., "Coupling light into few-mode optical fibres i: The diffraction limit," *Opt. Express* **15**, 1443–1453 (Feb 2007).

[8] "Astrophotonics: astronomy and modern optics," *The Astronomy and Astrophysics Review* **29** (Sep 2021).

[9] Fan, X., Wang, D., Cheng, J., Yang, J., and Ma, J., "Few-mode fiber coupling efficiency for free-space optical communication," *J. Lightwave Technol.* **39**, 1823–1829 (Mar 2021).

[10] Brüning, R., Zhang, Y., McLaren, M., Duparré, M., and Forbes, A., "Overlap relation between free-space laguerre gaussian modes and step-index fiber modes," *J. Opt. Soc. Am. A* **32**, 1678–1682 (Sep 2015).

[11] Simon Ellis, Jonathan Bland-Hawthorn, S. L.-S., "General coupling efficiency for fibre fed astronomical instruments," *J. Opt. Soc. Am. B* (2021).

[12] Diab, M., Dinkelaker, A. N., Davenport, J., Madhav, K., and Roth, M. M., "Starlight coupling through atmospheric turbulence into few-mode fibres and photonic lanterns in the presence of partial adaptive optics correction," *Monthly Notices of the Royal Astronomical Society* **501**, 1557–1567 (12 2020).

[13] Winston, R., Jiang, L., and Ricketts, M., "Nonimaging optics: a tutorial," *Adv. Opt. Photon.* **10**, 484–511 (Jun 2018).

[14] Miller, D. A. B., "Waves, modes, communications, and optics: a tutorial," *Adv. Opt. Photon.* **11**, 679–825 (Sep 2019).

[15] Chahine, Y. K., Tedder, S. A., Staffa, J., and Vyhnalek, B. E., "Optimal efficiency for passively coupling partially coherent light into mode-limited optical waveguides," *J. Opt. Soc. Am. A* **38**, 1732–1743 (Dec 2021).

[16] Bastiaans, M., "The wigner distribution function applied to optical signals and systems," *Optics Communications* **25**(1), 26–30 (1978).

[17] Wigner, E., "On the quantum correction for thermodynamic equilibrium," *Phys. Rev.* **40**, 749–759 (Jun 1932).

[18] Peyrin, F. and Prost, R., "A unified definition for the discrete-time, discrete-frequency, and discrete-time/frequency wigner distributions," *IEEE Trans. Acoust. Speech Signal Process.* **34**, 858–867 (1986).

[19] O'Toole, J. and Boashash, B., "Fast and memory-efficient algorithms for computing quadrating time-frequency distributions," *Applied and Computational Harmonic Analysis* **35**(2), 350–358 (2013).

[20] Claasen, T. A. C. M. and Mecklenbrauker, W. F. G., "The wigner distribution - a tool for time-frequency signal analysis," (1980).

[21] O'Toole, J., "Discrete quadratic time-frequency distributions: definition, computation, and a newborn electroencephalogram application," (2009).

[22] Testorf, M., Hennelly, B., and Ojeda-Castañeda, J., [*Phase-space optics: fundamentals and applications*], McGraw-Hill Education (2010).

[23] Simon, R. and Mukunda, N., "Optical phase space, wigner representation, and invariant quality parameters," *J. Opt. Soc. Am. A* **17**, 2440–2463 (Dec 2000).

[24] Alonso, M. A., "Wigner functions in optics: describing beams as ray bundles and pulses as particle ensembles," *Adv. Opt. Photon.* **3**, 272–365 (Dec 2011).

[25] Schmidt, J. D., [*Numerical Simulation of Optical Wave Propagation with Examples in MATLAB*], vol. PM199, SPIE, Bellingham, Washington (2010).

[26] Leon-Saval, S. G., Argyros, A., and Bland-Hawthorn, J., "Photonic lanterns: a study of light propagation in multimode to single-mode converters," *Opt. Express* **18**, 8430–8439 (Apr 2010).

[27] Dragoman, D., "Phase space representation of modes in optical waveguides," *Journal of Modern Optics* **42**(9), 1815–1823 (1995).

[28] Fried, D. L., "Optical resolution through a randomly inhomogeneous medium for very long and very short exposures," *J. Opt. Soc. Am.* **56**, 1372–1379 (Oct 1966).

[29] Heidbreder, G., "Image degradation with random wavefront tilt compensation," *IEEE Transactions on Antennas and Propagation* **15**(1), 90–98 (1967).

[30] Guyon, O., "Phase-induced amplitude apodization of telescope pupils for extrasolar terrestrial planet imaging," *A&A* **404**(1), 379–387 (2003).